ANNALS OF GEOPHYSICS, 69, 2, SA223, 2026; doi:10.4401/ag-9479
OPEN ACCESS

Synthesizing Virtual and Real-Height Ionograms using IONOLAB-RAY

Esra Erdem Kocak*,[1], Feza Arikan[2]

(1) Aselsan, Rehis, Ankara, Turkey
(2) Hacettepe University, Electrical and Electronics Engineering, Ankara, Turkey

Article history: received October 30, 2025; accepted February 26, 2026

Abstract

IONOLAB-RAY is a modular ray-tracing toolbox that models electromagnetic wave propagation through a realistic, time-varying ionosphere represented by a three-dimensional voxel-based grid. Within each voxel, refractive indices are computed from the full Appleton-Hartree formulation, accounting for anisotropy, magnetic field effects, and collisions. The physical parameters of the ionosphere are derived from background ionospheric model, which can be assimilated with Total Electron Content (TEC) data, allowing for the near real-time updating of the statistical model to reflect current ionospheric conditions. The system simulates both ordinary and extraordinary propagation modes under varying geophysical conditions. Designed for global and near real-time operation, IONOLAB-RAY can be executed for any position on Earth and for varying ionospheric states. Its user-friendly interface supports multiple-run simulations, allowing users to analyze wave propagation under different scenarios and explore the influence of input parameters such as signal frequency, elevation, and azimuth angle. For each computed ray path, the toolbox determines key physical parameters – attenuation, phase and group velocity, and total propagation delay – and generates both virtual and real-height ionograms. Real-height ionograms, derived from actual ray trajectories, provide essential insights into true reflection altitudes and ionospheric structure. Through its flexibility, physical accuracy, and operational efficiency, IONOLAB-RAY serves as a powerful framework for ionospheric modeling, propagation analysis, and space environment studies.

Keywords: Ionosphere; Ray Tracing; Ionogram Generation; Radio Wave Propagation; Ionospheric Modeling

---

1. Introduction

Understanding the propagation of electromagnetic waves through the ionosphere is essential for accurate modeling of radio communication, navigation, and remote sensing systems (Budden, 1988). The ionosphere acts as a natural propagation medium that bends, refracts, and reflects radio waves depending on its electron density distribution, magnetic field structure, and temporal variability. These characteristics, influenced by solar and geomagnetic activity, make the ionosphere highly dynamic and complex. Accurate simulation of this environment is therefore critical for improving signal reliability, system performance, and the interpretation of ionospheric measurements.

The ionosphere's inhomogeneous, anisotropic, and time-dependent nature poses significant challenges for modeling electromagnetic wave propagation. Its properties vary not only with altitude but also with latitude, longitude, local time, and solar conditions, creating a medium that is both dispersive and non-stationary. This complexity makes direct analytical solutions of Maxwell's equations impractical, motivating the use of ray-tracing techniques based on the geometrical-optics approximation (Haselgrove, 1955; Haselgrove and Haselgrove, 1960; Jones, 1966; Jones and Stephenson, 1975). Ray tracing enables the numerical computation of wave trajectories by treating the ionosphere as a refractive medium characterized by spatially varying parameters (Isaakidis and Xenos, 2004; Huang and Reinisch, 2006; Varrier, 2010).

Early studies, dating back to the 1930s, provided foundational models for electron density and refractive index, such as the Chapman layer model and the Appleton-Hartree equation, which remains the cornerstone for computing the refractive index in an anisotropic plasma (Chapman, 1939; Appleton, 1932; Hartree, 1931; Shkarofski, 1961; Budden, 1988). Later, global empirical models such as the International Reference Ionosphere (IRI) and its extensions to the plasmasphere (IRI-Plas) provided standardized electron density and temperature profiles derived from extensive observational data (Bilitza, 2001; Bilitza and Reinisch, 2008; Bilitza et al., 2014; Bilitza et al., 2022; Gulyaeva and Bilitza, 2012). These models, while robust, represent statistical medians and may not capture short-term ionospheric disturbances or localized structures.

Several ionospheric propagation models have been developed to support long-distance communication and frequency management, including Ionospheric Communications Analysis and Prediction (IONCAP), Voice of America Coverage Analysis Program (VOACAP), and Ionospheric Communications Enhanced Profile Analysis and Circuit (ICEPAC), which are based on empirical or semi-empirical approaches (Stewart, 1987; U.S. Department of Commerce, 2009; Tanyer and Erol, 1998). While these models have been effective for predicting average conditions, their performance degrades under disturbed or rapidly varying ionospheric states because they lack the ability to compute true three-dimensional wave trajectories and real-time variations in electron density.

Over the past decades, numerous ray-tracing algorithms and ionospheric modeling tools have been developed to study radio propagation and ionospheric characteristics. Classical tools such as Jones and Stephenson's early formulations provided the foundation for numerical ray tracing, while later systems, including PHaRLAP, IONORT, and other 3-D models, expanded the capability to simulate complex propagation paths under varying ionospheric conditions (Muldrew, 1959; Norman and Cannon, 1999; Li et al., 2010; Norman et al., 2012; Pietrella et al., 2023; Yan et al., 2011; Yaxin et al., 2012). However, many of these tools are limited by static model dependencies, restricted parameter control, or simplified geometries, which reduce their adaptability to near real-time and scenario-based applications.

While some ray-tracing models exist in the literature, the contribution of the present work does not lie in proposing a new physical formulation, but in the implementation, integration, and validation of a flexible and physically rigorous three-dimensional ray-tracing framework.

IONOLAB-RAY's specific contributions can be summarized as follows:

(i) a modular three-dimensional voxel-based structure that enables near real-time ray tracing of both ordinary and extraordinary wave modes, with refractive indices computed at each propagation step using the full Appleton-Hartree formulation, including electron cyclotron frequency, collision frequency, and anisotropy due to the geomagnetic field;

(ii) flexible integration with background ionospheric models and automatic assimilation of measured Total Electron Content (TEC) data to update the ionospheric state;

(iii) the capability to compute appropriate transmitter parameters, such as frequency, elevation, and azimuth, to enable point-to-point communication between two locations on Earth or in space;

(iv) the capability to compute communication parameters of attenuation, phase and group velocity and time delay.

(v) validation of the modeled propagation results using virtual-height ionograms derived from ionosonde measurements;

(vi) and the generation of real-height ionograms obtained directly from true three-dimensional ray trajectories, rather than from virtual-height inversion techniques.

To overcome these limitations, physically based ray-tracing algorithms have been introduced, offering higher spatial resolution and adaptability. The IONOLAB-RAY (Ionospheric Research Laboratory Ray Tracing Application) toolbox has been developed within this framework as a modular, user-friendly, and computationally efficient tool for simulating electromagnetic wave propagation in a realistic, time-varying ionosphere (Erdem, 2017; Erdem and

Arikan, 2017). The model represents the ionosphere as a three-dimensional voxel grid, within which the refractive index is calculated using the full Appleton-Hartree formulation, capturing the effects of anisotropy, collisions, and magnetic field orientation.

IONOLAB-RAY integrates all stages of ionospheric wave modeling – from environmental parameter computation to ray tracing and visualization – through two main modules: the preprocessor and the main processor. The preprocessor constructs the 3-D ionospheric grid and computes the required physical parameters for each voxel, while the main processor performs ray tracing using Snell's law across radial and lateral voxel interfaces. The software can be executed for any geographic region, date, and time, and supports near real-time operation by optionally assimilating Total Electron Content (TEC) data (Arikan et al., 2007a; Arikan et al., 2007b; Sayin et al., 2010; Erdem et al., 2015; Gulyaeva et al., 2013).

Beyond simulating propagation paths, IONOLAB-RAY calculates key parameters such as attenuation, phase and group velocities, and time delay, and generates both virtual and real-height ionograms. Real-height ionograms, derived directly from the computed ray trajectories, provide physically meaningful insight into reflection altitudes and ionospheric layer structure, bridging the gap between modeled results and ground-based ionosonde observations. Real-height ionograms, derived directly from actual ray trajectories, provide physically meaningful estimates of true reflection altitudes and enable direct comparison with ionosonde observations.

By combining physical rigor, operational efficiency, and extensive visualization capabilities, IONOLAB-RAY offers a comprehensive framework for studying ionospheric dynamics, analyzing communication links, and enhancing the accuracy of real-height ionogram interpretation under diverse geophysical conditions.

Several ionospheric ray-tracing tools have been developed in recent years to address different scientific and operational needs. Updated numerical implementations such as IONORT focus on improving stability and model fidelity for HF propagation studies, while analytical and semi-analytical approaches have been successfully applied to planetary atmospheres, radio occultation, and space-geodetic techniques (Bourgoin et al., 2019; Caruso et al., 2023; Zus et al., 2025). Other recent tools target specific applications such as satellite-based Earth observation missions, emphasizing computational efficiency and integration with orbit geometry (Molina et al., 2024).

In comparison, IONOLAB-RAY is designed as a flexible, voxel-based three-dimensional ray-tracing framework that emphasizes physical completeness, adaptability, and direct ionogram interpretation. The use of the full Appleton-Hartree formulation for both ordinary and extraordinary modes, combined with optional TEC assimilation, enables realistic modeling of anisotropy, dispersion, and disturbed ionospheric conditions. A key distinguishing feature of IONOLAB-RAY is its capability to generate real-height ionograms derived directly from true ray trajectories, rather than relying on inversion or virtual-height assumptions. This makes the tool particularly suitable for studies that aim to bridge numerical modeling with ground-based ionosonde observations and HF communication analysis.

The structure of this paper is organized as follows: Section 2 provides a concise overview of the IONOLAB-RAY algorithm, the details of which are documented in the corresponding thesis and earlier publication (Erdem, 2017; Erdem and Arikan, 2017). Section 3 presents applications related to wave propagation, while Section 4 focuses on the computation of key wave parameters using IONOLAB-RAY. Section 5 discusses the determination of the true reflection height and the local anisotropy of the ionosphere. Section 6 explains the generation of ionograms incorporating both virtual and real heights. Finally, Section 7 summarizes the conclusions and main findings of the study.

2. Brief Review of IONOLAB-RAY

IONOLAB-RAY is an advanced algorithm specifically crafted to model the propagation of waves in the ionosphere, accounting for its anisotropic, inhomogeneous, and time-dependent characteristics (Erdem, 2017).

The inhomogeneous structure of the ionosphere is represented as a three-dimensional spherical grid composed of voxels as shown in Fig. 1. Each voxel corresponds to a finite region of space within which ionospheric plasma parameters – such as electron density, collision frequency, and geomagnetic field components – are assumed to be locally homogeneous. This voxelized approach allows precise spatial representation of the ionosphere's horizontal and vertical gradients and enables accurate modeling of wave refraction and reflection processes. The user-defined ionospheric region is constructed by specifying explicit geographical and vertical boundaries together with the desired spatial resolution. For global simulations, these limits can be set to $-180° \leq \varphi \leq 180°$ for longitude (φ), $-90° \leq \theta \leq 90°$ for latitude (θ). The ionospheric altitude range can be defined as $h_{min} \leq h \leq h_{max}$. Minimum and maximum height can depend on the model used representing the ionosphere, in this study they can be

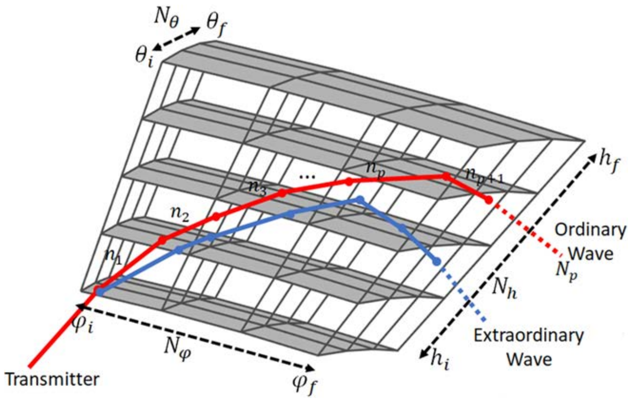

Figure 1. Wave propagation through 3D voxel model of ionosphere.

accepted 80 km and 20200 km respectively. For regional studies, narrower user-defined boundaries can be selected. This selected region is then discretized into height steps and latitude-longitude slices, each constituting a 3D spherical voxel with an adaptive resolution. The grid resolution is not required to be uniform. Adaptive meshing allows denser voxel distribution in regions with strong ionospheric gradients and coarser discretization in more homogeneous areas.

Ray tracing in IONOLAB-RAY is based on a geometrical-optics approach using simple geometric construction rather than continuous numerical integration of ray equations. The algorithm utilizes ray tracing principles based on Snell's Law to calculate the wave propagation path. The wave propagation originated from the transmitter and enters the 3D voxel structure. Snell's Law is applied at the locally plane radial or lateral boundary of the voxel. When a ray reaches a voxel boundary, the refractive index corresponding to the adjacent voxel is used to compute the new propagation direction. In this manner, ray bending is approximated by successive refractions across voxel boundaries, providing an efficient and physically consistent representation of wave propagation through a spatially varying medium. Both ordinary and extraordinary wave modes are generated when the incident wave enters the anisotropic ionospheric medium. These modes are traced independently throughout the voxel grid, allowing polarization-dependent propagation effects and geomagnetic field influences to be fully represented. The ray is propagated until it leaves the 3D region defined by the user or reaches to the Earth surface.

This voxel-based refraction strategy provides a balance between physical realism and computational efficiency, enabling three-dimensional ray tracing with near real-time performance while preserving the essential physics of ionospheric wave propagation.

Consequently, in this study, the ray tracing method is employed to simulate the propagation of waves. Spherical electric field ($\boldsymbol{E}$) wave expression is given in (1),

$$\boldsymbol{E}(\boldsymbol{r}) = \boldsymbol{E_o}\frac{1}{4\pi r}\exp(-\boldsymbol{k}\cdot\boldsymbol{r}) = \boldsymbol{E_o}\frac{1}{4\pi r}\exp(-\boldsymbol{\alpha}\cdot\boldsymbol{r})\exp\,(-\mathrm{j}\boldsymbol{\beta}.\boldsymbol{r}) \tag{1}$$

where $\boldsymbol{E_0}$ is polarization vector. The wave number, $\mathbf{k}$, attenuation constant, $\boldsymbol{\alpha}$, and propagation constant, $\boldsymbol{\beta}$, are defined as

$$\mathbf{k} = \hat{\boldsymbol{k}}k_o(Re\{n\} + jIm\{n\}) \tag{2}$$

$$\boldsymbol{\alpha} = \hat{\boldsymbol{k}}k_o Im\{n\} \tag{3}$$

$$\boldsymbol{\beta} = \hat{\boldsymbol{k}}k_o Re\{n\} \tag{4}$$

and n is the refractive index. The refractive index when the wave is not in the ionosphere is equal to $n = 1$ and $k_o = \omega\sqrt{\varepsilon_o\mu_o}$. Here, ω is the transmitter carrier frequency, ε_0 and μ_0 are permittivity and permeability of free space, respectively.

The refractive index, which is the most critical parameter of this intricate structure, is calculated by employing the Appleton-Hartree equation at each step of the ray tracing process through the voxels (Appleton, 1932; Hartree, 1931; Budden, 1988). The refractive index is assumed to be constant within each voxel and is recalculated only when the ray enters a new voxel. The Appleton-Hartree equation incorporates parameters such as electron cyclotron frequency, collision frequency, and components of the geomagnetic field, effectively capturing the anisotropy inherent in the ionosphere. This equation effectively captures the spatio-temporal variations and spatio-temporal dispersive nature of the ionosphere and ensures the generation of both ordinary and extraordinary waves.

Each date, time and longitude, latitude, height combination within the 3D user-defined region is assigned a lexicographical index (Sayin et al., 2008). The components of the Appleton-Hartree equation for each lexicographical index are calculated in the preprocess, except θ the angle between propagation vector and direction of geomagnetic field. The angle θ is calculated through propagation path at every step of refraction or reflection at the borders of the voxels contacted.

All over this paper and in Eq. (5), parameters computed during the preprocessing stage for each lexicographical index are denoted by the subscript l, whereas voxels encountered along the ray path are indexed as n_p. p^{th} step of wave propagation which is given by n_p is calculated with respect to the ionosphere parameters obtained for corresponding l^{th} lexicographic index.

The Appleton-Hartree equation (Appleton, 1932; Hartree, 1931) is given in (5)

$$n_l{}^2(n_p) = 1 - \frac{X}{1 - jZ_l - \dfrac{Y_l{}^2\,(\sin\theta(n_p))^2}{2(1 - X_l - jZ_l)} \pm \left[\dfrac{Y_l{}^4\,(\sin\theta(n_p))^4}{4(1 - X_l - jZ_l)^2} + Y_l{}^2(\cos\theta(n_p))^2\right]^{\frac{1}{2}}} \tag{5}$$

where,

$$X_l = N_{e_l} e^2/\varepsilon_0 m_l \omega^2 = f_{N_l}^2/f^2 \tag{6}$$

$$Y_l = eB_l/m_l\omega = f_{h_l}/f \tag{7}$$

$$Z_l = f_{v_l}/f \tag{8}$$

and $n_l{}^2$ is the square of refractive index, N_{e_l}, is electron density, f_{N_l} is plasma frequency, f is operation frequency, B_l is magnitude of geomagnetic field, $\theta(n_p)$ is angle between propagation vector $\mathbf{k}_l\,(n_p)$ and direction of geomagnetic field $\boldsymbol{B}_l$; f_{h_l} is cyclotron frequency and f_{v_l} is collision frequency, ω is the transmitter carrier frequency, e is electron charge, m_l is electron mass, ε_0 is free space dielectric constant and j is the imaginary unit. Incident wave which enters anisotropic media is divided into two waves called ordinary and extraordinary waves. The plus sign of operator '±' denotes the refractive index for ordinary wave and minus sign is for extraordinary wave.

To establish the physical parameters of the ionosphere at a given time and for the position of each voxel, any ionosphere background model can be integrated to IONOLAB-RAY. In this study IONOLAB-RAY draws data from the latest version of IRI-Plas software available when IONOLAB-RAY was developed (Gulyaeva and Bilitza, 2012). Total Electron Content (TEC) data can be assimilated to IRI-Plas, to introduce realistic modifications to the ionosphere model, particularly in storm conditions (Erdem et al., 2015). In this study, components of geomagnetic field are calculated with IGRF-13 (International Geomagnetic Reference Field, 13th generation) model (Thébault et al., 2021) and mass of ions is calculated with NRLMSISE (Naval Research Laboratory Mass Spectrometer and Incoherent Scatter Radar Extended) model (Picone et al., 2002). IONOLAB-RAY is flexible to be integrated other available models.

As shown in Fig. 2, IONOLAB-RAY is composed of preprocess and main process parts. In preprocess, the user defines the geographic region of interest by specifying the latitude and longitude boundaries, along with the desired spatial resolution of the ionospheric voxel grid. Temporal parameters, including the simulation date(s) and time(s), are also provided as inputs. The model optionally incorporates Total Electron Content (TEC) data to enhance realism and temporal accuracy.

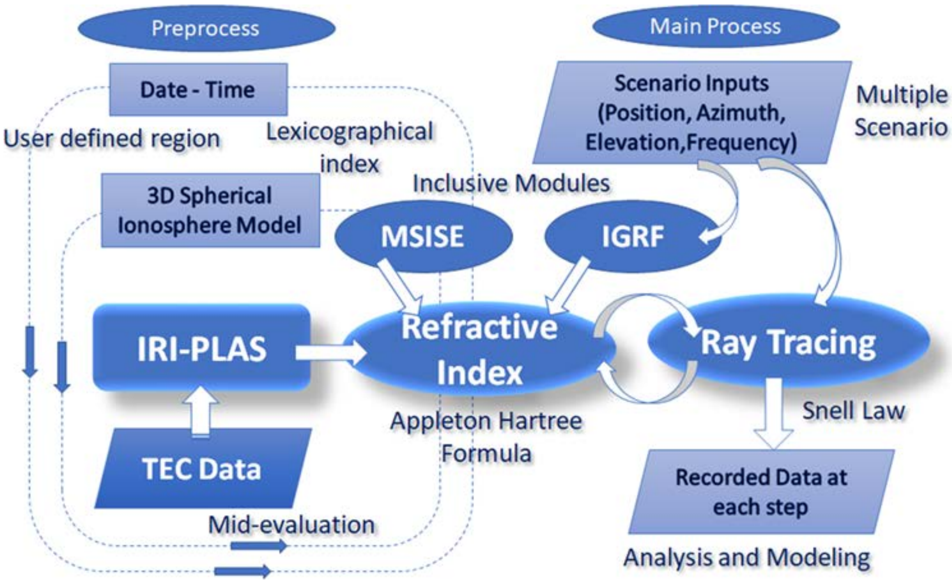

Figure 2. IONOLAB-RAY Algorithm Diagram.

For each voxel, and for each defined date and time, ionospheric and environmental parameters are computed using established empirical models. The resulting parameters – such as electron density, ion and neutral composition, temperature profiles, and geomagnetic field strength – are stored in lexicographical index for efficient access during the main computation. Electron density forms the core of the ionospheric model, while collision frequency is derived from the density and temperature of ionized and neutral species. The local cyclotron frequency is determined from the magnitude of the geomagnetic field within each voxel. These parameters collectively define the physical environment through which the rays will propagate.

In the main process part, the user runs the scenario with respect to the given the transmitter location, transmission frequency, azimuth and elevation angles, and the operational date and time. The geomagnetic field vector is first computed at the transmitter's location, and the wave is initiated as a ray propagating in free space until it intersects the ionospheric boundary. At this point, the ray splits into ordinary and extraordinary components, which are then traced independently.

Ray propagation within the ionosphere is computed voxel by voxel. At each step, the angle between the local geomagnetic field and the ray direction is determined, and the refractive index is calculated using the parameters generated during preprocessing via the full Appleton-Hartree formulation. Depending on the refractive gradient, the ray may either penetrate the ionosphere or be refracted and reflected back toward the Earth. If reflection occurs, the returning ray is propagated under free-space conditions after leaving the ionospheric boundary.

This two-stage structure allows IONOLAB-RAY to efficiently combine physical realism with computational flexibility, enabling users to perform detailed, scenario-based analyses of wave propagation under diverse ionospheric conditions.

IONOLAB-RAY employs a script-based functional user-friendly interface, simplifying the input process for both single and multiple runs. The design provides maximum flexibility for scientific applications, allowing users to effortlessly input parameters for their simulations. Users define all simulation parameters directly through function calls, enabling full control over scenario configuration and easy automation of multiple-run analyses. Additionally, the software features 2D and 3D plot capabilities, enabling users to visualize and analyze the outputs effectively. Some examples of these scripts are given in Fig. 3.

IONOLAB-RAY is also designed to be run on a CPU, allowing users to execute multiple scenarios in near real-time (Kacar, MSc Thesis, 2018). The efficiency of the algorithm is highlighted by the fact that the preprocess operation, conducted for a specific date, time, and region of interest (divided into 5 steps in latitude and longitude each and 41 steps in height), takes less than 8 seconds. This impressive speed is achieved on a standard PC equipped with an Intel Core i7-9750H CPU @ 2.59 GHz processor and 16 GB RAM. Moreover, the main process, contingent on the number of voxels traversed by the wave path, typically completes in less than 0.1 seconds on the same type of PC. The computational cost of IONOLAB-RAY primarily depends on the number of voxels defining the ionospheric

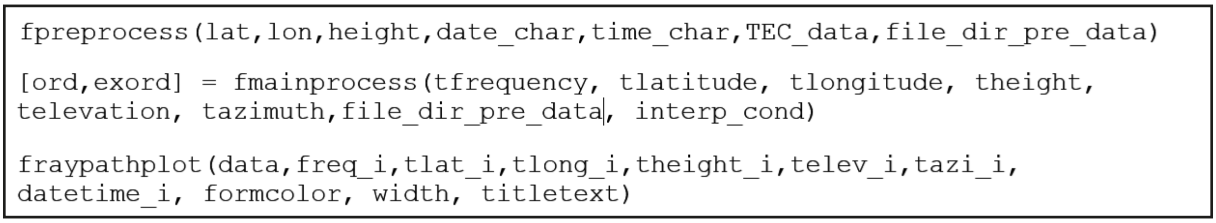

```
fpreprocess(lat,lon,height,date_char,time_char,TEC_data,file_dir_pre_data)

[ord,exord] = fmainprocess(tfrequency, tlatitude, tlongitude, theight,
televation, tazimuth,file_dir_pre_data, interp_cond)

fraypathplot(data,freq_i,tlat_i,tlong_i,theight_i,telev_i,tazi_i,
datetime_i, formcolor, width, titletext)
```

Figure 3. Example of the script-based user interface of IONOLAB-RAY.

grid and on the number of voxel interfaces crossed by a given ray path. Since each voxel is assumed to be locally homogeneous, and all ionospheric parameters are computed at the voxel center (latitude, longitude, height), the computational load per voxel is independent of its physical dimensions. The refractive indices and ionospheric parameters are precomputed during the preprocessing stage, the main ray-tracing process scales approximately linearly with the number of voxels encountered along the propagation path. Compared to numerical ray-tracing approaches based on continuous integration, this voxel-based refraction strategy provides competitive computational performance and enables near real-time execution on standard CPU hardware, as reported in similar ray-tracing studies. The availability of a dedicated software tool version further enhances user flexibility and accessibility. Overall, the swift processing times and CPU compatibility make IONOLAB-RAY a practical and efficient solution for users engaging in diverse simulation scenarios.

3. Applications For Wave Propagation

IONOLAB-RAY enables the simulation of broadcasts from an antenna situated at a user-defined location, encompassing diverse azimuth and elevation directions. This simulation leverages ray tracing algorithms to compute the input parameters of point-to-point communication, precisely defining the rays reaching the receiver location within a specified region.

A set of example communication scenarios is conducted between Chicago and New York City. The main aim of this study is to identify representative HF communication scenarios that may occur between New York and Chicago for selected days and times, and to demonstrate the capability of IONOLAB-RAY to compute the corresponding propagation and communication parameters. A total of 31 viable scenarios were identified within the tested dataset. In order to keep the manuscript at a reasonable length, a representative subset of these scenarios is presented and discussed in detail. The selected cases are intended to illustrate the performance and outputs of the model rather than to provide a systematic parametric sensitivity analysis, which is beyond the scope of the present paper. The transmitter is positioned in Chicago with coordinates [41.88°N, 87.62°W], while the receiver is situated in New York with coordinates [40.73°N, 73.94°W]. Two specific dates are chosen to represent distinct ionospheric conditions: the 17th of April 2011 for a geomagnetically quiet day and the 25th of October 2011 for a geomagnetically disturbed day. Furthermore, to capture a comprehensive range of scenarios, simulation times are set at 05:00 UT and 17:00 UT, representing midnight and midday conditions, respectively. A 3D spherical voxel structure is formed for a region of interest between 38°N-43°N latitude, 70°W-90°W longitude, 80 km-500 km height, with latitude and longitude resolution of 0.5° and height resolution of 1 km. So that number of latitudes, $N_\theta = 11$, number of longitudes, $N_\varphi = 41$ and number of altitudes, $N_h = 421$, which makes the total number of voxels 189,871. IRI-Plas model is assimilated with corresponding TEC data.

In the present implementation, neutral atmospheric refraction below approximately 80 km is not included, and wave propagation from the ground-based transmitter to the lower ionospheric boundary is assumed to occur along straight paths ($n = 1$); for the HF frequencies and elevation angles considered in this study, the resulting deviation in the initial incidence angle and reflection height is expected to be small and negligible compared to ionospheric refraction effects.

Multiple scenarios are run with variation of

- frequency from 3 MHz to 15 MHz with a resolution of 3 MHz
- elevation angle of transmitted wave from 5° to 60° with a resolution of 5°
- azimuth angle of transmitted wave towards the receiver from 90° to 96° with a resolution of 2°.

The investigation extends to both ordinary and extraordinary wave propagation paths, analyzing those arriving within a narrow latitude range of ±0.5° and a longitude range of ±0.5° centered around the receiver position. In these simulations of scenario sets, 31 distinct paths achieve point-to-point communication between Chicago and New York is successfully established through comprehensive simulations of all broadcasts originating from the transmitter. This thorough examination accounts for various propagation paths and ensures a detailed understanding of the communication dynamics between the two locations under different conditions and scenarios.

Prior to analyzing the representative wave paths, we first summarize the ionospheric conditions associated with the selected scenario dates (17 April 2011 – quiet; 25 October 2011 – disturbed) and times (05:00 and 17:00 UT). The corresponding Kp and Dst index values are provided below to quantitatively substantiate the geomagnetic classification.

- 17 April 2011, 05:00 UT, Kp: 0.3, Dst: 3 nT;
- 17 April 2011, 17:00 UT, Kp: 1, Dst: 4 nT;
- 25 October 2011, 05:00 UT, Kp: 5.7, Dst: −134 nT;
- 25 October 2011, 17:00 UT, Kp: 2, Dst: −57 nT.

In Fig. 4, electron density profiles at the center location of the latitude and longitude interval of region of interest are given. The vertical electron density profiles are obtained directly from the background ionospheric model used in IONOLAB-RAY, namely the IRI-Plas model assimilated with TEC data. As expected, daytime conditions exhibit higher electron densities throughout the E-F region and a lower effective reflection height for a given frequency, while nighttime profiles are depleted and more weakly structured. It should be noted that the propagating wave encounters continuously varying electron density profiles along its entire trajectory. The profiles shown in Fig. 4 therefore represent illustrative vertical snapshots extracted at a representative location, rather than the exact density distribution experienced at every point along the ray path.

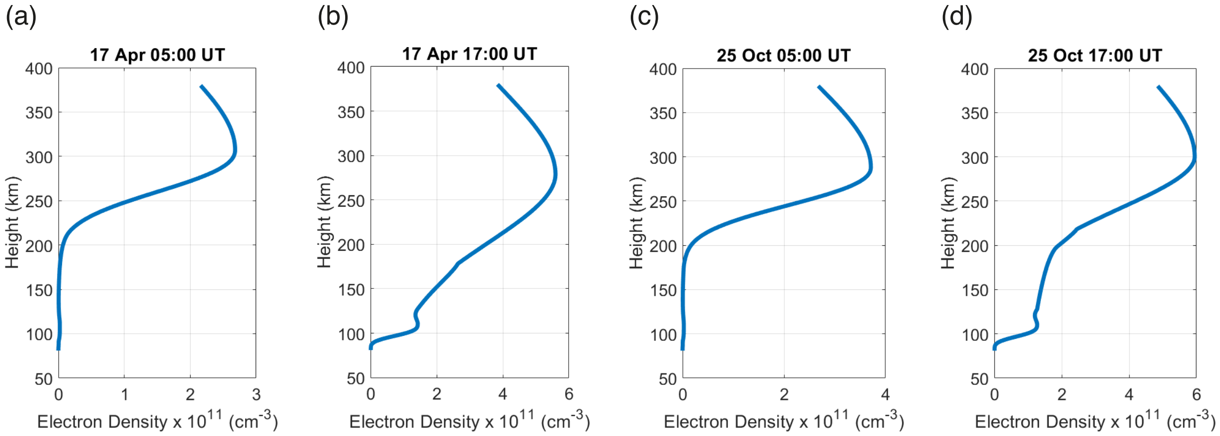

Figure 4. Ionospheric electron density distribution for the selected scenario dates. Nighttime conditions correspond to 05:00 UT and daytime conditions correspond to 17:00 UT on 17 April 2011 (geomagnetically quiet) and 25 October 2011 (geomagnetically disturbed).

From the full set of scenarios, a subset was selected for result presentation and discussion. The results of the selected example ordinary and extraordinary wave paths are tabulated in Table 1 and plotted in Fig. 5. The communication parameters explained in the next chapter will also be discussed regarding to these selected scenarios. On this table T represents time delay in ms and A represents attenuation in V/m which will be introduced in the next chapter. The results of time delay and attenuation are inserted in this table to to avoid repeating the table in the following chapter.

Plots (a) and (b) in Fig. 5 illustrate the three-dimensional ray paths of the ordinary (O) and extraordinary (E) wave modes, respectively, simulated for the eight scenarios summarized in Table 1. Each scenario represents a distinct combination of frequency, elevation, azimuth, and local time conditions on 17 April 2011 (geomagnetically quiet) and 25 October 2011 (disturbed).

Table 1. Wave Path Scenarios.

Sce. #	Date	Time (UT)	O/E	Freq. (MHz)	Ele. (°)	Azi. (°)	Path Length (km)	T (ms)	A (×10-07) (V/m)
1	17-Apr	5:00	O	3	20	90	1194.8	4.03	5.48
2	17-Apr	17:00	O	9	20	92	1190.4	4.14	0.27
3	25-Oct	5:00	O	6	20	94	1258.6	4.24	7.10
4	25-Oct	17:00	O	6	5	90	1192.3	3.98	1.36
5	17-Apr	5:00	E	3	20	90	1216.7	4.14	2.12
6	17-Apr	17:00	E	6	5	90	1173.8	3.92	0.73
7	25-Oct	5:00	E	6	20	92	1286.5	4.35	6.59
8	25-Oct	17:00	E	12	30	94	1344.4	4.80	2.86

In plot (a), corresponding to ordinary-mode propagation (Scenarios 1-4), the ray paths demonstrate clear dependencies on both frequency and solar illumination conditions. Lower-frequency waves (e.g., 3 MHz in Scenario 1) are refracted more strongly, reaching higher altitudes and shorter ground ranges before returning to Earth. In contrast, higher-frequency waves (e.g., 9 MHz in Scenario 2) penetrate deeper into the ionosphere with reduced curvature, resulting in longer skip distances. The daytime simulations (17:00 UT) show lower reflection heights due to enhanced ionization, while nighttime conditions (05:00 UT) produce higher reflection points and more extended propagation paths.

Plot (b) presents extraordinary-mode propagation (Scenarios 5-8). The general patterns are similar, but the extraordinary waves exhibit slightly greater reflection altitudes and longer trajectories for equivalent frequencies. This difference arises from the influence of the geomagnetic field, which modifies the refractive index and polarization characteristics of the E-mode. At higher frequencies (e.g., 12 MHz in Scenario 8), rays penetrate deeper before reflection, consistent with reduced refractive effects at shorter wavelengths.

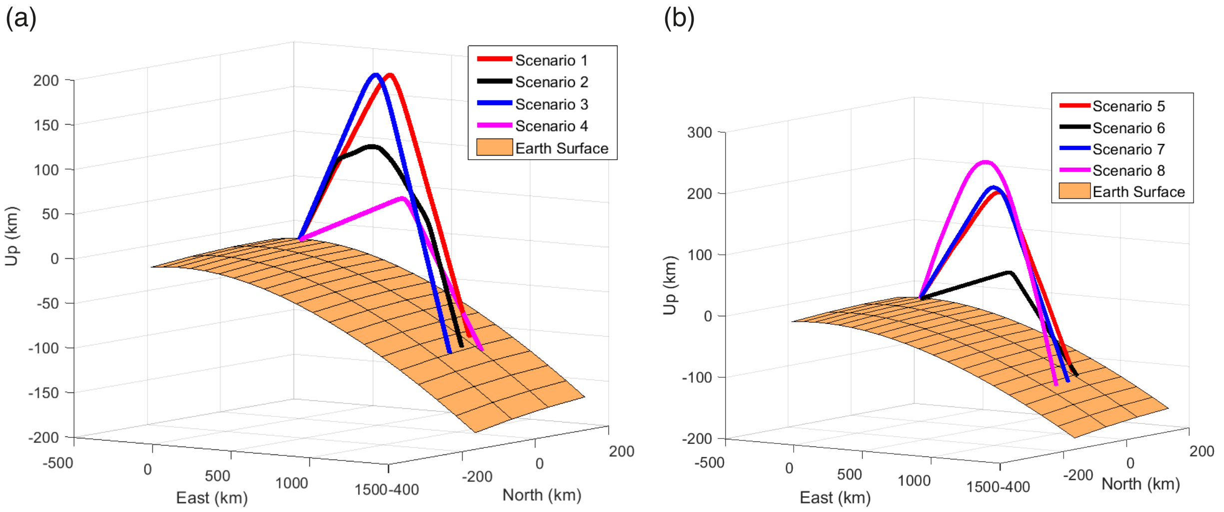

Figure 5. Wave propagation paths for example scenarios. (a) Scenarios 1-4, Ordinary Waves; (b) Scenarios 5-8, Extraordinary Waves.

Overall, the results confirm that frequency, time of day, and wave mode all exert strong control over ray curvature and reflection altitude. IONOLAB-RAY successfully captures these dependencies, demonstrating its capability to model realistic ionospheric propagation under both quiet and disturbed conditions.

Although only eight representative scenarios are presented in the manuscript, a total of 31 ray propagation scenarios were analyzed. Across all scenarios, ray paths exhibit consistent and physically meaningful curvature primarily controlled by frequency, time of day, and propagation mode. Lower-frequency and nighttime cases show stronger bending and higher reflection altitudes, whereas higher-frequency and daytime conditions result in flatter trajectories with deeper ionospheric penetration. Extraordinary-mode rays consistently reflect at slightly higher altitudes than ordinary-mode rays due to ionospheric anisotropy and geomagnetic field effects. The eight scenarios presented in the manuscript are therefore characteristic of the broader propagation behavior modeled by IONOLAB-RAY.

4. Applications for Communication Parameters

A very important capability of IONOLAB-RAY is to compute wave parameters such as attenuation, phase velocity, group velocity, and time delay, that are crucial inputs for the HF communication channel model. This enhancement stands as a significant advantage over alternative algorithms, as it empowers IONOLAB-RAY to provide a more comprehensive understanding of the communication environment. These parameters play a pivotal role in shaping channel models, facilitating the development of critical insights necessary for achieving optimum communication performance.

It should be noted that the scenarios compared in this section are selected as representative examples from the tested dataset and are not intended to constitute a controlled parametric study. The observed differences arise from the combined influence of frequency, elevation angle, and propagation mode, and therefore individual parameter effects are not isolated here. The purpose of this comparison is to illustrate how attenuation, phase and group velocities and time delay evolve along realistic three-dimensional ray trajectories generated by IONOLAB-RAY, rather than to establish causal relationships between specific transmission parameters.

4.1 Attenuation

The wave propagating in the ionosphere undergoes attenuation due to the interaction between the wave and free electrons. In this study, attenuation is modeled only within the ionosphere and is attributed to electron-neutral and electron-ion collision processes; attenuation due to the neutral atmosphere below the ionosphere is not included, as it is generally negligible for HF frequencies compared to ionospheric absorption. The calculation of ionospheric attenuation is vital for many applications (Budden, 1988). In this paper the attenuation is calculated through the wave path under the given scenario conditions.

In the IONOLAB-RAY algorithm, since both the ordinary and extraordinary waves are traced, the attenuation for these components can be individually calculated. Derivation of the formulation for attenuation is given in the appendix, Eqs. (A1)-(A3). Components of attenuation factor for chosen scenarios, which are 2nd and 6th scenarios, given in the Table 1, are examined in this part of the chapter and the results are plotted in Fig. 6. Three components are evaluated and plotted with respect to number of voxel step n_p, where $1 \leq n_p \leq N_p$. N_p is the total number of voxels that the wave traces in the ionosphere. These components are

- Cumulative attenuation constant with respect to voxel number n_p, plotted with legend “alpha”
- Exponential term of attenuation factor up to n_pth voxel,

$$A_e(n_p) = \exp\left\{-\sum_{n_q=1}^{n_p} \alpha_l(n_q) r(n_q)\right\} \tag{9}$$

- and cumulative exponential term divided by path length up to n_pth voxel,

$$A_L(n_p) = \frac{1}{\sum_{n_q=1}^{n_p} r(n_p)} \exp\left\{-\sum_{n_q=1}^{n_p} \alpha_l(n_q) r(n_q)\right\} \tag{10}$$

In Table 1, the attenuation factor A, computed from the cumulative absorption along each propagation path, exhibits clear variations across the different simulation scenarios, reflecting the combined influence of frequency, wave mode, time of day, and ionospheric conditions. The results reveal noticeable variability across the scenarios, reflecting the combined influence of frequency, propagation mode, time of day, and background ionospheric conditions. For the ordinary-mode (O) cases (Scenarios 1-4), the highest attenuation is observed in Scenario 3 (7.10 V/m), while the lowest value occurs in Scenario 2 (0.27 V/m). This indicates that attenuation is not governed by a single controlling parameter but rather emerges from the interplay between operating frequency, ray geometry, and the prevailing ionospheric state.

For the extraordinary-mode (E) cases (Scenarios 5-8), attenuation values also exhibit significant variation. Scenario 7 shows the strongest attenuation (6.59 V/m), whereas Scenario 6 yields the weakest attenuation (0.73 V/m). Scenario 8 results in a moderate attenuation level (2.86 V/m), lying between these two extremes. These differences can be attributed to polarization-dependent wave-plasma interactions and the influence of the geomagnetic field, which modify the refractive index and affect collisional damping along the propagation path.

Overall, the attenuation parameter demonstrates the complex and non-monotonic dependence of ionospheric absorption on multiple environmental and transmission parameters. Rather than following a simple frequency- or time-dependent trend, the results emphasize the importance of three-dimensional propagation geometry and localized ionospheric structure. These findings confirm that IONOLAB-RAY is capable of capturing such coupled effects and providing physically meaningful estimates of wave power loss along realistic propagation paths.

In Fig. 6, the plots (a) and (b) illustrate the variation of attenuation-related parameters along the ray path as a function of the voxel index n_p. The blue dotted curve (α) represents the local attenuation constant, while the red dashed (A_e) and black solid (A_L) lines correspond to the exponential term of the attenuation factor and its normalized cumulative form, respectively, defined by Eqs. (12) and (13). The vertical axis of the plots is given in logarithmic scale.

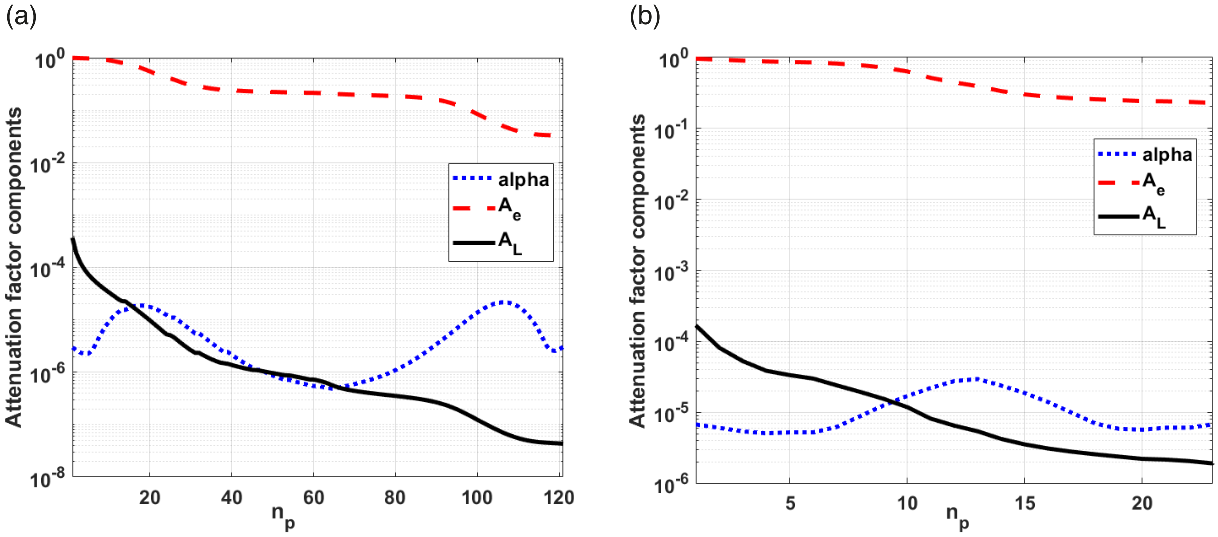

Figure 6. Electron Attenuation and its components for selected wave paths. (a) Scenario 2, (b) Scenario 6.

4.2 Phase Velocity and Group Velocity

IONOLAB-RAY's voxel-based computation allows for detailed phase velocity and group velocity mapping along complex three-dimensional ray trajectories, providing a more realistic understanding of wave behavior and propagation dynamics under varying ionospheric conditions. Derivation of the formulation for phase and group velocity is given in the appendix, Eqs. (A4)-(A7). In the algorithm, the phase and group velocities are computed for both ordinary and extraordinary waves in each voxel. In Fig. 7, plots (a) and (b) present the variation of phase and group velocities along the ray paths for the ordinary-mode (Scenario 4) and extraordinary-mode (Scenario 8) waves, respectively. Both velocities were computed voxel by voxel along the ray path.

In both figures, the phase velocity (black dashed line) and group velocity (red solid line) exhibit complementary behavior, reflecting the dispersive nature of the ionospheric plasma. The group velocity decreases sharply in the region where the refractive index approaches a minimum, corresponding to the vicinity of the reflection point, while the phase velocity simultaneously increases, forming a characteristic mirrored pattern. This inverse relationship is consistent with the theoretical condition $v_p v_g = c^2$ for electromagnetic waves in a lossless dispersive medium, where v_p is phase velocity, v_g is group velocity, and c is the speed of light in free space.

For Scenario 4 (O-mode, 6 MHz), the total path length is shorter and the variations in both velocities are more moderate, reflecting the lower operating frequency and smaller elevation angle. The minimum group velocity occurs near the midpoint of the ray path, indicating strong refraction where the wave transitions from the E-region toward the F-region reflection height.

In Scenario 8 (E-mode, 12 MHz), the group velocity shows a deeper and broader reduction, while the phase velocity peak is more pronounced. This is attributed to both the higher operating frequency and the magnetic field interaction characteristic of the extraordinary mode, which enhance anisotropy and dispersion. The increased elevation angle also extends the total propagation path, resulting in a greater number of voxels and smoother variation along the trajectory.

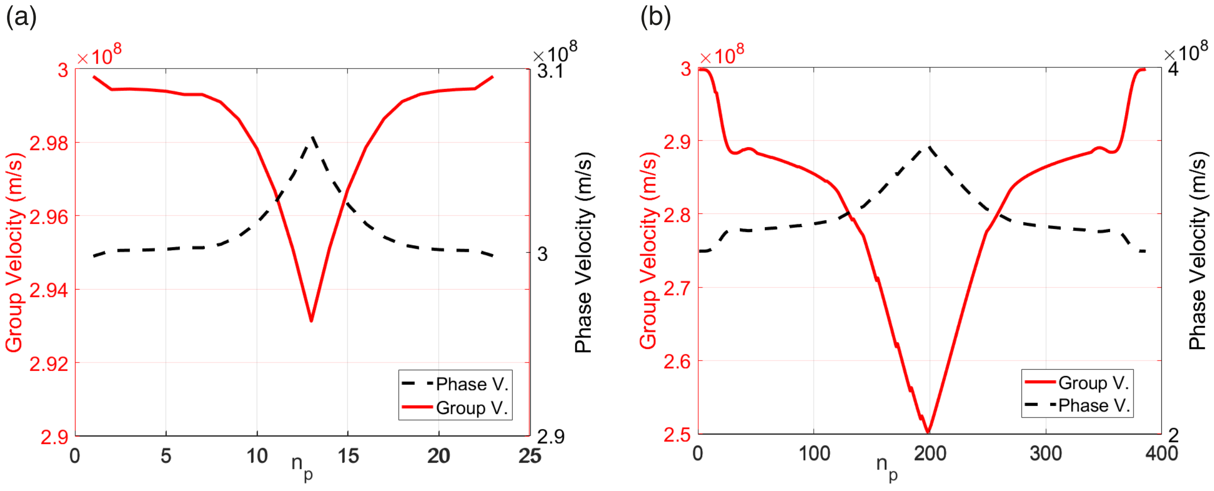

Figure 7. Group and phase velocity for selected ordinary wave paths (a) Scenario 4 (b) Scenario 8.

4.3 Time Delay

IONOLAB-RAY's voxel-based computation allows for detailed time delay calculation for each step. Derivation of the formulation for time delay is given in the appendix, Eqs. (A8)-(A9). For the selected scenarios given in Table 1, time delay results are given under the column represented by 'T(ms)'. Across all cases, T ranges from about 3.92 to 4.80 ms, reflecting changes in ray geometry, turning height, and dispersion along the path. In general, larger turning heights and longer in-ionosphere path lengths yield greater delay; where group velocity dips near the reflection region, T increases.

Ordinary-mode cases (1-4) show modest spread. Nighttime or disturbed conditions tend to increase delay: scenario 3 (25-Oct 2011, 05:00, 6 MHz) has the largest O-mode delay at 4.24 ms, exceeding the daytime 6 MHz case (scenario 4, 3.98 ms). The 3 MHz nighttime case (scenario 1, 4.03 ms) is slightly lower than the 9 MHz daytime case (scenario 2, 4.14 ms), indicating that frequency alone does not control T; diurnal ionization and the launch geometry also matter.

Extraordinary-mode cases (5-8) exhibit a wider spread and the highest overall value. The nighttime 6 MHz case (scenario 7) gives 4.35 ms, larger than its daytime counterpart at similar frequency/elevation (scenario 6, 3.92 ms), consistent with higher turning heights and stronger dispersion at night. Scenario 5 (3 MHz, night) yields 4.14 ms, close to the O-mode behavior at comparable conditions.

Figure 8 presents the cumulative time delay along the ray trajectory as a function of the voxel index. This representation allows tracking how the group delay accumulates progressively as the wave propagates through different ionospheric regions. In all cases, the monotonic increase reflects the continuous reduction of group velocity due to refractive effects associated with spatial variations in electron density. Steeper portions of the curves correspond to regions of stronger refraction, typically occurring near the turning point of the ray.

In Fig. 8(a), Scenarios 2 and 6 yield total delays of approximately 4.14 ms and 3.92 ms, respectively, consistent with the values reported in Table 1. Although both scenarios correspond to daytime conditions, they differ in frequency, elevation angle, and propagation mode. Consequently, the observed differences in cumulative delay result from the combined influence of these parameters rather than from a single controlling variable.

Figure 8(b) compares Scenarios 4 and 8. Scenario 8 exhibits a larger total delay (~4.80 ms) distributed over a longer voxel sequence, indicating a more extended propagation path. This behavior arises from the joint effects of higher frequency, larger elevation angle, and extraordinary-mode propagation, which together modify both the ray geometry and the refractive properties of the medium. Scenario 4, in contrast, shows a shorter cumulative delay (~3.98 ms), reflecting its different trajectory characteristics.

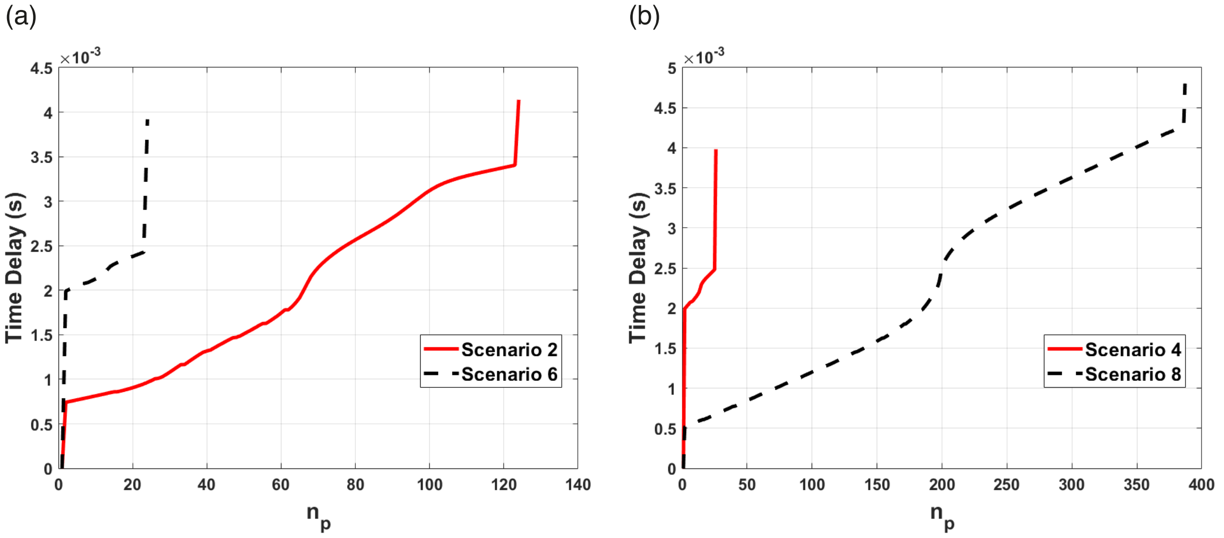

Figure 8. Cumulative time delay for selected wave propagation paths (a) Scenario 2 and 6, (b) Scenario 4 and 8.

5. True Height and Local Anisotropicity

The reflection points of the ordinary and extraordinary waves of the 31 scenarios introduced in Section 3 are recorded and given in Fig. 9. Blue and red stars indicate the reflection points for ordinary and extraordinary waves respectively. The reflection point of the wave is the maximum height that the wave reaches in the ionosphere.

In plot (a), the reflection points are plotted in latitude-longitude coordinates. The points cluster along the east-west propagation path between Chicago and New York, showing that the waves reflect within a relatively narrow longitudinal range centered over the defined region of interest. The proximity of the O- and E-mode reflection points (blue and red markers, respectively) indicates that both modes follow similar horizontal trajectories. However, minor separations between them demonstrate the effect of magnetic field orientation and anisotropy, causing lateral separations of up to approximately 1° in longitude, depending on propagation mode and ionospheric conditions between the ordinary and extraordinary ray paths.

Plot (b) presents the same reflection points in latitude-height space. The plot reveals that most reflections occur between altitudes of approximately 100 km and 300 km, corresponding to the E- and F-region layers of the ionosphere. The extraordinary waves (red circles) generally reach slightly higher altitudes than the ordinary waves (blue points) under the same conditions, consistent with their larger refractive index and reduced effective plasma frequency. This difference reflects the distinct polarization and interaction of each mode with geomagnetic field.

The spatial distribution of reflection points demonstrates that IONOLAB-RAY accurately captures both the vertical and horizontal variability of ionospheric reflection behavior. The results highlight how propagation mode, frequency, and ionospheric anisotropy jointly influence the true reflection height and lateral displacement of the

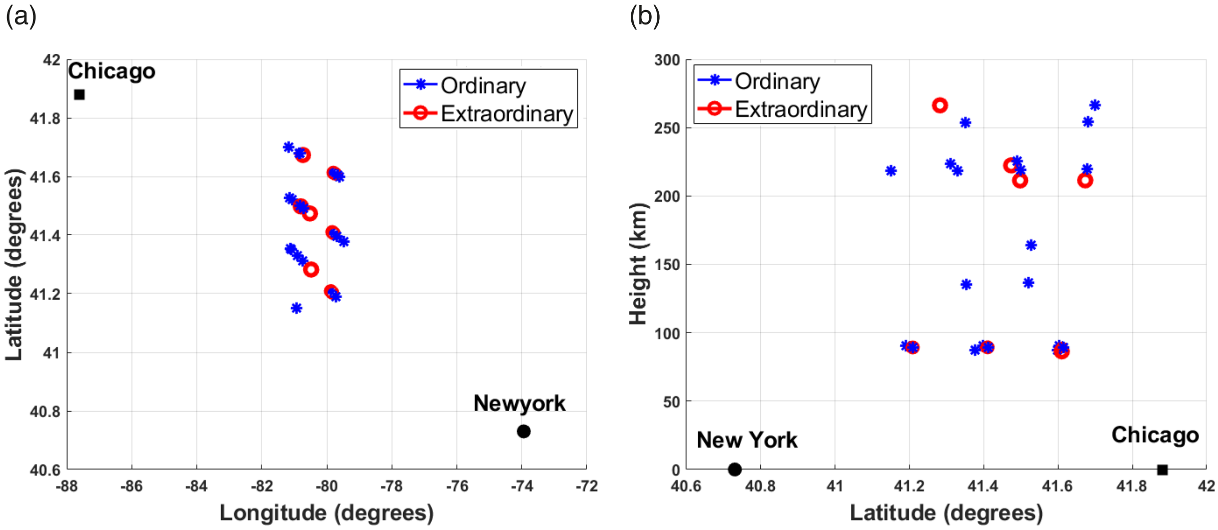

Figure 9. Reflection points of ordinary (blue) and extraordinary (red) waves for the 31 simulation scenarios: (a) latitude-longitude projection and (b) latitude-height projection.

signal path. Although 31 simulations were performed, some markers overlap because several ray paths reach their maximum reflection heights at nearly identical locations. Consequently, fewer visually distinguishable points appear in the figure.

These reflection height distributions form the foundation for constructing real-height ionograms, which depict the actual altitudes of ionospheric reflection as a function of frequency. By integrating the reflection data from multiple scenarios, IONOLAB-RAY enables the generation of both virtual and real-height ionograms, providing a direct comparison between theoretical modeling and observational data. The following section presents examples of these ionograms and discusses their interpretation in relation to ionosonde measurements.

6. Ionogram Generation with Virtual and Actual Heights

Ionosondes determine reflection heights by transmitting vertically directed radio pulses and measuring the round-trip travel time of the returned echoes. The recorded height is obtained by assuming that the wave propagates at the speed of light along a straight vertical path and is instantaneously reflected at a single altitude. However, in reality, radio waves propagating in the ionosphere experience continuous refraction due to the gradual variation of the refractive index with altitude. As a result, the actual propagation path is curved and the group velocity is reduced relative to the speed of light. Because these refractive effects are not explicitly accounted for in the time-to-height conversion, the inferred reflection altitude is systematically overestimated. The height obtained in this manner is therefore referred to as the virtual height, rather than the true physical reflection height.

An ionogram illustrates the relationship between the transmitted radio frequency and the corresponding apparent reflection height of ionospheric layers, from which the true reflection height can be derived. It is a fundamental diagnostic tool in ionospheric research and monitoring, providing key information on critical frequencies, layer structure, and overall ionospheric variability.

Within the IONOLAB-RAY framework, ionograms are produced in two complementary forms: virtual-height ionograms and real-height ionograms. The virtual height is computed under the assumption of vertical propagation with instantaneous reflection at the critical plasma frequency, neglecting refraction effects. The real height, on the other hand, is obtained directly from the three-dimensional ray-tracing computations, representing the true altitude at which the wave reverses direction in the ionosphere. This approach enables IONOLAB-RAY to connect traditional ionosonde observations with realistic propagation modeling.

To evaluate the consistency of IONOLAB-RAY with measured data, virtual heights are calculated and superimposed on the ionograms, while the reflection height for each frequency is extracted from the corresponding ray trajectory to construct the real-height ionogram. In this section, the modeled ionograms are compared with experimental observations from the Pruhonice and Grahamstown ionosondes to assess the model's performance in reproducing realistic ionospheric behavior under different geophysical conditions. For quasi-vertical ionogram simulations, the transmitter and receiver are colocated at the ionosonde station coordinates (Pruhonice: 50.0°N, 14.6°E; Grahamstown: 33.3°S, 26.5°E). Rays are launched within a narrow angular cone around 90°, and those returning within a 5 km radius of the transmitter location are considered received, representing the effective antenna footprint. All simulations presented for the Pruhonice and Grahamstown ionograms were performed using the IRI-Plas model assimilated with TEC data.

In Fig. 10, plots show measured ionograms recorded by the Pruhonice ionosonde and the IONOLAB-RAY simulations for 14 February 2015 at 13:00 and 17:00 UT. In each figure, the blue points represent the measured virtual heights, while the red points indicate the heights computed by IONOLAB-RAY for the same frequency range and geophysical conditions. The simulated virtual heights display good overall agreement with the ionosonde measurements, particularly in the E- and F-region reflections. At both local times, IONOLAB-RAY successfully reproduces the general curvature of the trace. Discrepancies are observed at higher frequencies are related to the finite angular and frequency resolution employed in the ray-launching scheme, as well as the numerical termination criteria used in the virtual height inversion procedure. Near the critical frequency, small changes in frequency and elevation angle lead to large variations in reflection height. Accurately resolving this regime

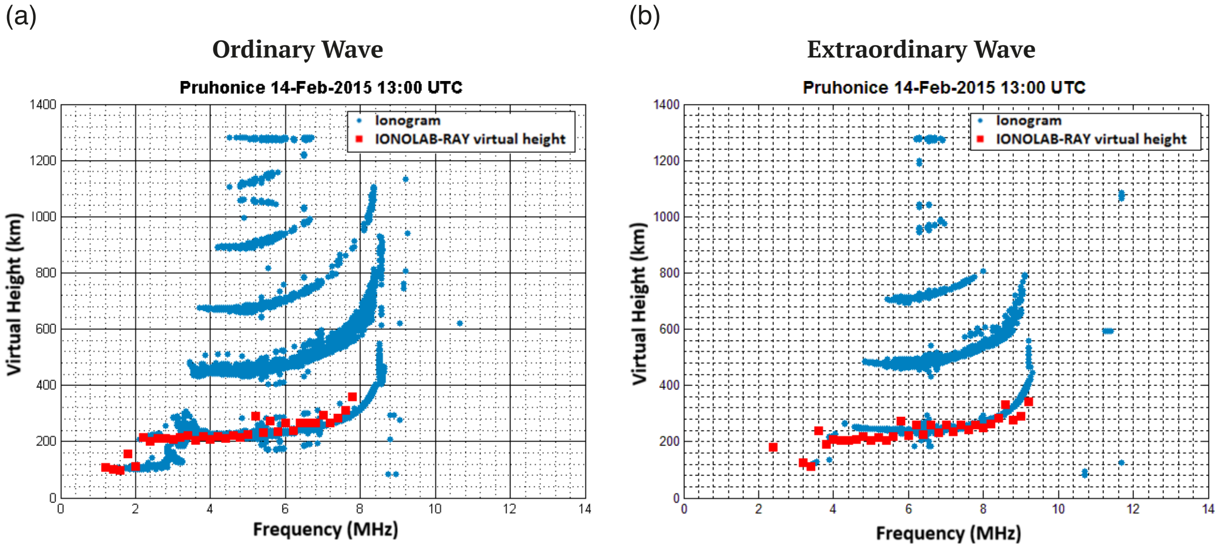
(a) Ordinary Wave

(b) Extraordinary Wave

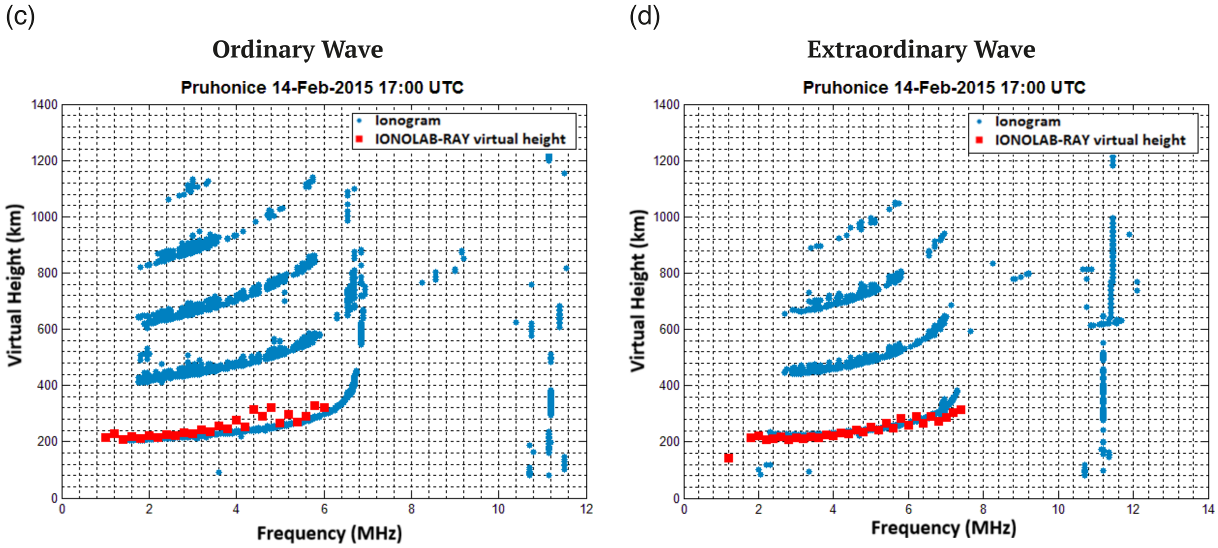
(c) Ordinary Wave

(d) Extraordinary Wave

Figure 10. Ionograms with virtual heights – Pruhonice, 14-Feb-2015 (a) 13:00 UT, ordinary wave; (b) 13:00 UT, extraordinary wave; (c) 17:00 UT, ordinary wave; (d) 17:00 UT, extraordinary wave; the blue points represent the measured virtual heights, while the red points indicate the virtual heights computed by IONOLAB-RAY.

would require significantly finer sampling in both frequency and ray elevation, which would substantially increase the computational cost. There are features associated with multi-hop propagation paths involving successive ground-ionosphere reflections (e.g., 1F, 2F, and 3F hops). Such higher-order reflections are not explicitly modeled in the current single-hop ray-tracing configuration, which primarily focuses on the first-order reflection.

The results confirm that the model's computation of virtual heights can reliably reproduce the frequency-height relationship obtained from standard ionosonde measurements. This compatibility establishes confidence in the model's capability to extend ionogram interpretation to real-height calculations, which are presented in the Fig. 11.

In Fig. 11, plots (a) and (b) present the measured ionogram from the Pruhonice ionosonde and the corresponding IONOLAB-RAY simulations, including both virtual and real (actual) heights for 14 February 2015 at 13:00 UT. In these plots, blue points represent the observed ionosonde data, red squares denote the IONOLAB-RAY calculated virtual heights, and green diamonds indicate the real reflection heights obtained through three-dimensional ray-tracing computations. The virtual heights calculated by IONOLAB-RAY, shown by red dots, exhibit closer agreement with the ionosonde ionogram measurements because ionosonde-recorded heights are derived under the assumption that the wave propagates vertically at the speed of light and is instantaneously reflected at a single altitude, referred to as the virtual height. The results show that the real-height curve follows the general trend of the ionosonde trace but lies systematically below the virtual-height curve, as expected. In reality, radio waves propagating in the ionosphere experience continuous refraction and reduced group velocity due to the gradual variation of the refractive index with altitude. Consequently, the real height provides a more accurate representation of the physical reflection altitude.

For the presented cases, the difference between the modeled real-height reflection points and the corresponding ionosonde-derived virtual heights is typically on the order of several tens of kilometers. Such differences are commonly reported in ionospheric propagation studies and arise from differences in measurement definitions, oblique versus vertical propagation assumptions, and model uncertainties in electron density representation. A simple root-mean-square (RMS) difference computed over the analyzed frequencies yields values on the order of a few tens of kilometers, indicating reasonable agreement given the inherent variability of the ionosphere.

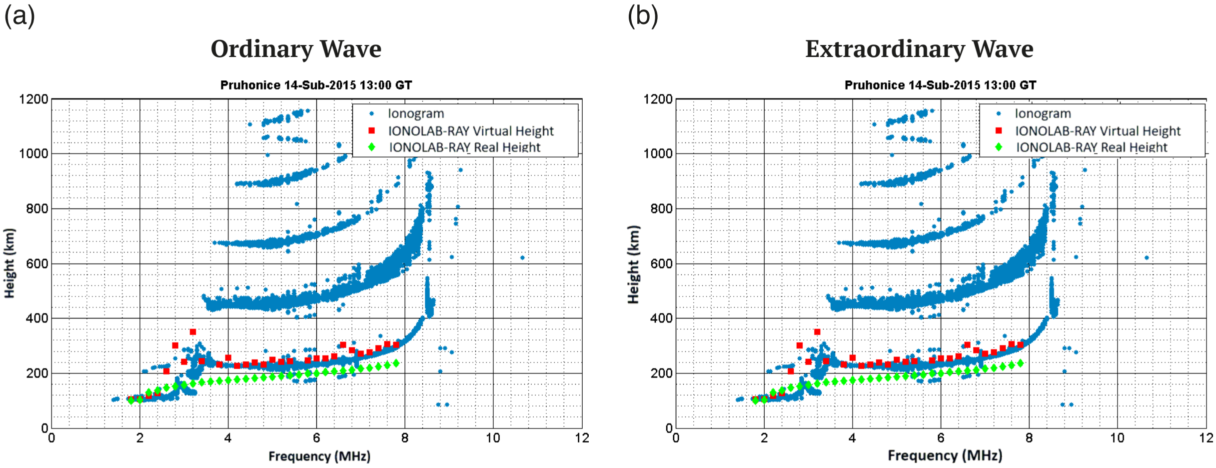
(a) Ordinary Wave

(b) Extraordinary Wave

Figure 11. Ionograms with actual heights – Pruhonice 14-Feb-2015 (a) 13:00 UT, ordinary wave; (b) 13:00 UT, extraordinary wave; blue points represent the observed ionosonde measurements, red squares denote the virtual heights calculated by IONOLAB-RAY, green diamonds indicate real reflection heights calculated by IONOLAB-RAY.

The results are extended for Grahamstown Ionosonde. The ionograms shown in Fig. 12 correspond to the typical output format of a Digisonde Portable Sounder (DPS-4D) operated at the Grahamstown station. In these plots, the red traces represent ordinary mode (O-mode) reflections, while the green traces indicate extraordinary mode (E-mode) reflections. The thin solid black curve corresponds to the true-height electron density profile automatically derived by the ionosonde scaling software ARTIST (Automatic Real-Time Ionogram Scaler and Trace; Reinisch and Galkin, 2011). The vertical axis denotes the virtual height (h′) in km, whereas the horizontal axis represents the plasma frequency in MHz. In Fig. 12 plots (a) and (b) show measured ionograms from the Grahamstown ionosonde (red/green trace families) with IONOLAB-RAY overlays at 12:00 and 15:00 UT on 17 Apr 2011. Blue squares are the model's virtual heights and magenta diamonds are the model's actual reflection heights derived from 3-D ray tracing. For both times, IONOLAB-RAY reproduces the main E/F-region traces and their curvature with frequency. The virtual-height overlay tracks the measured virtual trace envelopes, while the real-height curve sits below, as expected when refraction along the true path is accounted for.

(a)

Grahamstown (GR13L) – 17 April 2011, 12:00 UT

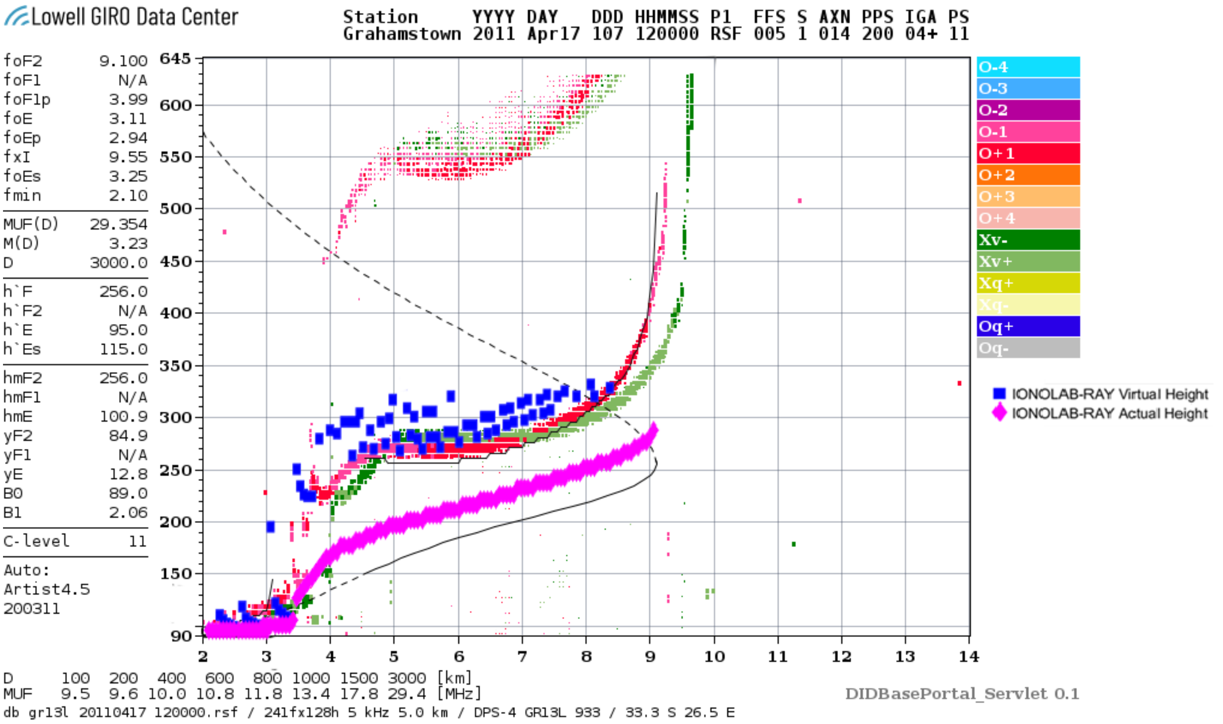

(b)

Grahamstown (GR13L) – 17 April 2011, 15:00 UT

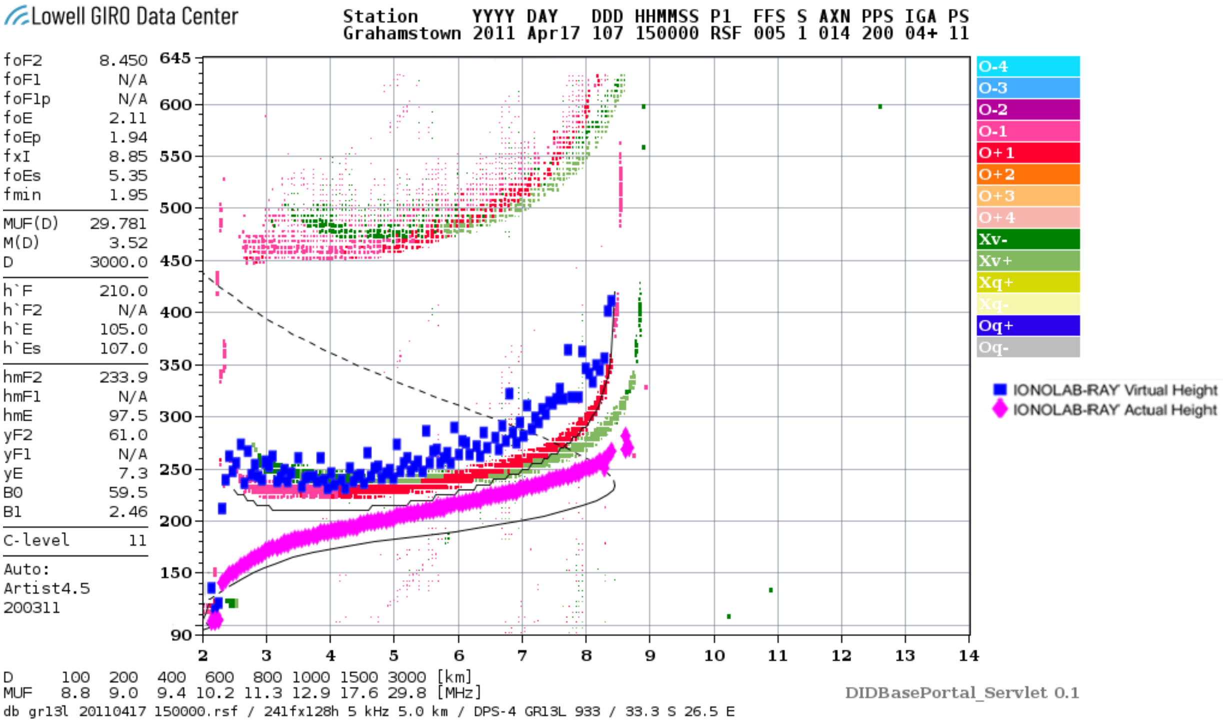

Figure 12. Ionograms with virtual and actual heights-Grahamstown (South Africa), 17 April 2011 (a) 12:00 UT (b) 15:00 UT.

A noticeable difference is observed between the true-height profile automatically derived by the ARTIST software (thin black curve) and the true heights obtained from IONOLAB-RAY (magenta diamonds). While ARTIST relies directly on scaling the experimental ionogram traces and is therefore affected by measurement noise and scaling ambiguities, IONOLAB-RAY derives true heights independently through physics-based 3-D ray tracing driven by the IRI-Plas model. Due to the fundamentally different nature of these approaches, determining which profile is more accurate is not straightforward. The observed discrepancy highlights both the limitations of automatic ionogram scaling and the sensitivity of model-based reconstructions to background ionospheric assumptions.

The Pruhonice ionosonde data used in this study were obtained in numerical format through a collaborative research project with the Institute of Atmospheric Physics, Czech Academy of Sciences. This enabled direct extraction and numerical plotting of virtual height values together with IONOLAB-RAY simulation results. Therefore, Fig. 10 and Fig. 11 present reconstructed ionogram traces derived from digital data, with ordinary and extraordinary modes displayed separately for clarity. In contrast, ionograms from the Grahamstown station were available only as image files, and no numerical data access was possible. Accordingly, in Fig. 12, IONOLAB-RAY outputs were overlaid directly onto the original ionogram screenshots, preserving the native layout showing both O- and E-mode traces simultaneously.

The overall correspondence between the simulated and measured ionograms mainly reflects the accuracy of the IRI-Plas model assimilated with TEC in representing the vertical electron density structure, while the IONOLAB-RAY algorithm successfully propagates the radio waves through this background medium by correctly computing the associated time delays and ray paths. The inclusion of both virtual and real heights allows detailed examination of how refraction and anisotropy influence the apparent reflection levels observed by ionosondes. These results demonstrate that IONOLAB-RAY can accurately transform modeled propagation data into physically meaningful real-height ionograms, providing valuable support for interpretation and validation of ionospheric observations.

7. Conclusion

In this study, a comprehensive three-dimensional ray-tracing framework, IONOLAB-RAY, has been presented to model electromagnetic wave propagation through the ionosphere with high physical accuracy and flexibility. The toolbox integrates a voxel-based ionospheric representation with the full Appleton-Hartree formulation to account for anisotropy, magnetic field effects, and collisions. Its two-stage structure – comprising a preprocessing phase for environmental modeling and a main process for dynamic ray computation – enables efficient and realistic simulations under varying geophysical and geomagnetic conditions. All simulations were performed using the IRI-Plas model assimilated with TEC data, ensuring that realistic background electron density conditions were incorporated.

The results demonstrate that IONOLAB-RAY effectively reproduces both ordinary and extraordinary wave trajectories, providing detailed insight into reflection mechanisms and local anisotropy in the ionosphere. Computed propagation parameters, including attenuation, phase and group velocities, and time delay, are consistent with theoretical expectations and demonstrate the system's capability for accurate channel characterization. The reflection height analyses show clear differentiation between ordinary and extraordinary modes, validating the model's ability to capture the ionospheric birefringent structure.

IONOLAB-RAY's ionogram generation feature successfully links modeled results to experimental observations. Comparisons with ionograms from the Pruhonice and Grahamstown stations reveal strong consistency between the measured and simulated virtual heights, while the real-height ionograms derived from ray trajectories provide valuable corrections to apparent reflection levels. The agreement observed in virtual heights mainly reflects the quality of the assimilated IRI-Plas model, whereas IONOLAB-RAY ensures physically consistent propagation by accurately computing ray paths and time delays. These results confirm that the tool can accurately reconstruct true reflection heights, supporting improved interpretation of ionosonde data and realistic modeling of ionospheric behavior.

Overall, IONOLAB-RAY offers a robust computational platform for studying ionospheric radio-wave propagation and its effects on communication and navigation systems. Its near real-time capability, user-friendly interface, and adaptability to different input models make it a valuable tool for both scientific research and operational applications in space weather and ionospheric monitoring. Future work will focus on systematic parametric sensitivity studies and the inclusion of multi-hop propagation scenarios to further extend the model's applicability.

References

Appleton, E. V. (1932). Wireless studies of the ionosphere, J. Inst. Electr. Eng., 71, 430, 642-650, doi:10.1049/jiee-1.1932.0144.

Arikan, F., O. Arikan and C. B. Erol (2007a). Regularized estimation of TEC from GPS data for certain midlatitude stations and comparison with the IRI model, Adv. Space Res., 39, 867-874, doi:10.1016/j.asr.2006.06.013.

Arikan, F., O. Arikan and I. Sayin (2007b). Synthetic TEC mapping with ordinary and universal kriging, in International Conference on Recent Advances in Space Technologies, RAST, 14-16 June 2007, Istanbul, Turkey, IEEE, 39-43.

Bilitza, D. (2001). International Reference Ionosphere 2000, Radio Sci., 36, 261-273, doi:10.1029/2000RS002432.

Bilitza, D. and B. W. Reinisch (2008). International Reference Ionosphere 2007: Improvements and new parameters, Adv. Space Res., 42, 599-609, doi:10.1016/j.asr.2007.07.048.

Bilitza, D., D. Altadill, Y. Zhang, C. Mertens et al. (2014). The International Reference Ionosphere 2012 – a model of international collaboration, J. Space Weather Space Clim., 4, A07, doi:10.1051/swsc/2014004.

Bilitza, D., M. Pezzopane, V. Truhlik, D. Altadill et al. (2022). The International Reference Ionosphere model: A review and description of an ionospheric benchmark, Rev. Geophys., 60, e2022RG000792, doi:10.1029/2022RG000792.

Bourgoin, A., J. Saillard and G. M. C. Fischer (2019). Analytical ray tracing in planetary atmospheres, Astronomy & Astrophysics, 625, A138, doi:10.1051/0004-6361/201834962.

Budden, K. G. (1988). The Propagation of Radio Waves, Cambridge University Press, Cambridge, 669, ISBN:0-521-32196-7.

Caruso, A., E. Cardellach and M. Garcia-Fernandez (2023). Radio occultation data analysis with analytical ray-tracing, Radio Sci., 58, e2023RS007740, doi:10.1029/2023RS007740.

Chapman, S. (1939). The atmospheric height distribution of band absorbed solar radiation, Proc. Phys. Soc., 51, 93-109, doi:10.1088/0959-5309/51/1/312.

Erdem, E. (2017). Electromagnetic Wave Propagation Model and Simulation in Ionosphere, PhD Thesis, Hacettepe University, Turkey.

Erdem, E. and F. Arikan (2017). IONOLAB-RAY: A wave propagation algorithm for anisotropic and inhomogeneous ionosphere, Turk. J. Electr. Eng. Comput. Sci., 25, 3, 1712-1723, doi:10.3906/elk-1602-119.

Erdem, E., F. Arikan, M. N. Deviren and I. Cor (2015). A model-based ray tracing algorithm for anisotropic and inhomogeneous ionosphere with GIM-TEC assimilation, in International Conference on Recent Advances in Space Technologies, RAST, 16-19 June 2015, Istanbul, Turkey, IEEE, 477-481.

Gulyaeva, T. L., X. Huang and B. W. Reinisch (2002). Plasmaspheric extension of topside electron density profiles, Adv. Space Res., 29, 825-831, doi:10.1016/S0273-1177(02)00037-2.

Gulyaeva, T. L. and D. Bilitza (2012). Towards ISO Standard Earth Ionosphere and Plasmasphere Model, NOVA Science Publishers, Hauppauge, NY, 194, ISBN:978-1-61470-956-3.

Gulyaeva, T. L., F. Arikan, M. Hernandez-Pajares and I. Stanislawska (2013). GIM-TEC adaptive ionospheric weather assessment and forecast system, J. Atmos. Sol. Terr. Phys., 102, 329-340, doi:10.1016/j.jastp.2013.06.011.

Hartree, D. R. (1931). The propagation of electromagnetic waves in a refracting medium in a magnetic field, Proc. Camb. Philos. Soc., 27, 1, 143-162, doi:10.1017/S0305004100009440.

Haselgrove, J. (1955). Ray theory and a new method of ray tracing, Proc. Phys. Soc. Lond., 23, 355-364.

Haselgrove, C. B. and J. Haselgrove (1960). Twisted ray paths in the ionosphere, Proc. Phys. Soc. Lond., 75, 357-363, doi:10.1088/0370-1328/75/3/304.

Huang, X. and B. W. Reinisch (2006). Real-time HF ray tracing through a tilted ionosphere, Radio Sci., 41, RS5S90, doi:10.1029/2005RS003378.

Isaakidis, S. A. and T. D. Xenos (2004). Wave propagation and reflection in the ionosphere: an alternative approach for ray path calculations, Prog. Electromagn. Res., 45, 201-215, doi:10.2528/PIER03070401.

Jones, R. M. (1966). A three-dimensional ray tracing computer program, ESSA Technical Report IER, 17-ITSA, 17, Government Printing Office, Washington, DC, USA.

Jones, R. M. and J. J. Stephenson (1975). A versatile three-dimensional ray tracing computer program for radio waves in the ionosphere, U.S. Department of Commerce, Washington, DC, USA.

Kacar, A. (2018). GPU parallel computing of ray tracing algorithms for modeling wave propagation in the ionosphere, MSc Thesis, Department of Electrical and Electronics Engineering, Hacettepe University, Ankara, Turkey.

Li, W., D. Su and Z. Yan (2010). Three-dimensional ray tracing in International Reference Ionosphere, in Antennas and Propagation and EM Theory (ISAPE) Symposium, 29 Nov-2 Dec 2010, Guangzhou, China, IEEE, 584-587.

Molina, M. G., M. A. Gende and M. Brunini (2024). Modern ionospheric ray tracer for Earth observation satellite missions, IEEE, J. Sel. Top. Appl. Earth Obs. Remote Sens., 17, 1-12, doi:10.1109/JSTARS.2024.3421509.

Muldrew, D. B. (1959). An ionospheric ray-tracing technique and its application to a problem in long-distance radio propagation, IRE Trans. Antennas Propag., 7, 393-396, doi:10.1109/TAP.1959.1144705.

Norman, R. J. and P. S. Cannon (1999). An evaluation of a new two-dimensional analytic ionosphere ray tracing technique: segmented method for analytic ray tracing (SMART), Radio Sci., 34, 489-499, doi:10.1029/98RS01788.

Norman, R. J., J. Le Marshall, B. A. Carter and C. S. Wang (2012). A new pseudo three-dimensional segment method analytical ray tracing (3-D SMART) technique, IEEE Trans. Antennas Propag., 60, 5818-5824, doi:0.1109/TAP.2012.2214194.

Pietrella, M., M. Pezzopane, A. Pignatelli, A. Pignalberi et al. (2023). An Updating of the IONORT Tool to Perform a High-Frequency Ionospheric Ray Tracing, Remote Sens., 2, 15, 5111, doi:10.3390/rs15215111.

Picone, J. M., A. E. Hedin, D. P. Drob and A. C. Aikin (2002). NRLMSISE-00 empirical model of the atmosphere: Statistical comparisons and scientific issues, J. Geophys. Res., 107, A12, 1468, doi:10.1029/2002JA009430.

Reinisch, B. W. and I. A. Galkin (2011). Global ionospheric radio observatory, GIRO, EPS, 63, 377-381, doi:10.5047/eps.2011.03.001.

Sayin, I., F. Arikan and K. E. Akdogan (2010). Optimum temporal update periods for regional ionosphere monitoring, Radio Sci., 45, RS5008, doi:10.1029/2009RS004316.

Sayin, I., F. Arikan and O. Arikan (2008). Regional TEC mapping with random field priors and kriging, Radio Sci., 43, RS4018, doi:10.1029/2007RS003786.

Shkarofski, P. (1961). Generalized Appleton-Hartree equation for any degree of ionization and application to the ionosphere, Proc. IRE 49, 1857-1871, doi:10.1109/JRPROC.1961.287714.

Stewart, F. G. (1987). Ionospheric Communications Analysis and Prediction Program, IONCAP for Microcomputers, PB-87-130993/XAB, Boulder, Colorado, USA.

Tanyer, S. G. and C. B. Erol (1998). Broadcast analysis and prediction in the HF band, IEEE Trans. Broadcast, 44, 226-232, doi:10.1109/11.713075.

Thébault, E., C. D. Beggan, H. Amit, J. Aubert et al. (2021).International Geomagnetic Reference Field: The thirteenth generation, EPS, 73, doi:10.1186/s40623-020-01288-x.

U.S. Department of Commerce (2009). ICEPAC Technical Manual, NTIA/ITS, Boulder, Colorado, USA.

Varrier, N. R. (2010). Ray tracing analysis for the mid-latitude SuperDARN HF radar at Blackstone incorporating the IRI-2007 model, MSc Thesis, Virginia Tech, Blacksburg, VA, USA.

Yan, Z., G. Wang, G. Tian, W. Li et al. (2011). The HF channel EM parameters estimation under a complex environment using the modified IRI and IGRF model, IEEE Trans. Antennas Propag., 59, 1178-1183, doi:10.1109/TAP.2011.2122237.

Yaxin, Y., J. Niu and J. J. Simpson (2012). A 3D global Earth-ionosphere FDTD model including an anisotropic magnetized plasma ionosphere, IEEE Trans. Antennas Propag., 60, 3246-3256, doi:10.1109/tap.2012.2196937.

Zus, F., K. Balidakis, A. H. Dogan, R. Thundathil et al. (2025). DNS (v1.0): an open-source ray-tracing tool for space geodetic techniques, Geosci. Model Dev., 18, 4951-4964, doi:10.5194/gmd-18-4951-2025.

Appendix A.

A1. Computation of Attenuation

Attenuation factor in each voxel 'n_p' on the ray path is calculated by using

$$A(n_p) = \frac{1}{r(n_p)} \exp\{-\alpha_l(n_p) r(n_p)\} \tag{A1}$$

where in the $n_p{}^{\text{th}}$ voxel, $r(n_p)$ is the distance traced by the wave, and $\alpha_l(n_p)$ is the attenuation constant. Here, $1 \leq l \leq N_p$. N_p is the total number of voxels that the wave propagation path traces in the ionosphere (Budden, 1988).

Total wave path length (R) is defined as given in (A2).

$$R = r_{TI} + \sum_{n_p=1}^{N_p} r(n_p) + r_{IR} \tag{A2}$$

where, r_{TI} and r_{IR} are the wave path length from transmitter location to the ionosphere and from ionosphere to the receiver, respectively. Since neutral atmospheric refraction is neglected, the path segments r_{TI} and r_{IR} are assumed to be straight free-space paths with refractive index $n = 1$.

The total attenuation factor (A) is calculated by

$$A = \frac{1}{R} \exp\left\{-\sum\nolimits_{n_p=1}^{N_p} \alpha_l(n_p) r(n_p)\right\} \tag{A3}$$

where N_p is the total number of voxels through the wave path.

A2. Computation of Phase and Group Velocity

As a feature of IONOLAB-RAY,Phase velocity, ϑ_p of the propagating wave is calculated for each voxel 'n_p' along the ray path. Phase velocity defines the rate at which the phase of the wavefront advances and is directly related to the refractive index of the medium. Within the IONOLAB-RAY framework, the phase velocity at voxel n_p is computed using

$$\vartheta_p(n_p) = \frac{\omega}{\beta_l(n_p)} = \frac{c}{Re\{n_l(n_p)\}} \tag{A4}$$

where ω is the angular frequency, $B_l(n_p)$ represents the local propagation constant, $n_l(n_p)$ is the complex refractive index obtained from the Appleton-Hartree formulation, and c is the speed of light in free space (Budden, 1988).

In an anisotropic medium, to introduce group velocity, it is useful to introduce the refractive index surface, where the refractive index n is constant (Budden, 1988). In Fig. A1 the relationships between the magnetic flux density $\boldsymbol{B}_l(n_p)$, the wave vector $\boldsymbol{k}_l(n_p)$ and the group velocity $\vartheta_g(n_p)$ are given for each voxel n_p. $\theta_l(n_p)$ is the angle between $\boldsymbol{B}_l(n_p)$ and $\boldsymbol{k}_l(n_p)$. $\delta_l(n_p)$ is the angle between $\boldsymbol{\vartheta_g}(n_p)$ and $\boldsymbol{k}_l(n_p)$.

Group velocity in an anisotropic medium with respect to the geometry given in Fig. 1 is

$$\vartheta_g(n_p) \cos \delta_l(n_p) = \partial\omega / \partial k_l(n_p) \tag{A5}$$

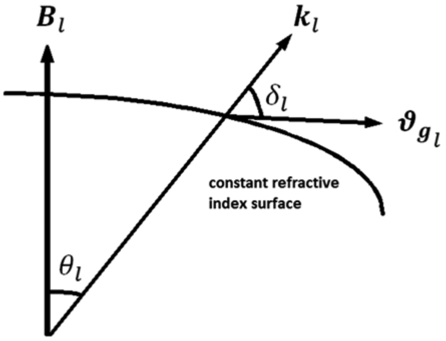

Figure A1. Definitions for group velocity in voxel l.

Here, the angle $\delta_l$is defined by

$$\tan\delta_l(n_p) = \frac{1}{n_l(n_p)}\frac{\partial n_l(n_p)}{\partial\theta_l(n_p)} \tag{A6}$$

Combining (16) and (17) gives

$$\vartheta_g(n_p) = \frac{c}{\cos\delta_l(n_p)\left[\frac{\partial\left(\omega n_l(n_p)\right)}{\partial\omega}\right]} \tag{A7}$$

A3. Computation of Time Delay

Time delay, $t_l$in each voxel, ‘n_p’ is calculated as

$$t(n_p) = \frac{r(n_p)}{\vartheta_g} \tag{A8}$$

The total time delay (T) between the transmitter and the receiver is computed as follows

$$T = t_{TI} + \sum_{n_p=1}^{N_p} t(n_p) + t_{IR} \tag{A9}$$

where, t_{TI} and t_{IR} are the time delay from transmitter location to the ionosphere of path length r_{TI} and from ionosphere to the receiver path length r_{IR}, respectively, assuming the wave travels with c outside ionosphere (Budden, 1988).

***CORRESPONDING AUTHOR:** **Esra ERDEM KOCAK**,
Aselsan, Rehis, Ankara, Turkey
e-mail: esraerd@gmail.com